Journal of Manufacturing Processes 124 (2024) 1193–1201

Contents lists available at ScienceDirect

Journal of Manufacturing Processes

journal homepage: www.elsevier.com/locate/manpro

A novel high-DPI and monodisperse droplet inkjet printhead with the piezoelectric cutter

Xucong Wang [a], Chaoran Liu [a,*], Defei Yao [b], Hongjian Lin [c], Jing Yu [b], Xin Tong [a], Zai Wang [a], Yi Wang [a], Weihuang Yang [a], Yu Gao [a], Serguei Lazarouk [d], Vladimir Labunov [d], Linxi Dong [a,*], Xiaoyuan Wang [b,*], Gaofeng Wang [a,*]

[a] Ministry of Education Engineering Research Center of Smart Microsensors and Microsystems, College of Electronics and Information, Hangzhou Dianzi University, Hangzhou 310018, PR China
[b] Zhejiang Key Laboratory of Ecological and Environmental Big Data, Hangzhou 321001, PR China
[c] Department of Electrical Engineering, City University of Hong Kong, 999077, PR China
[d] Belarusian State University of Informatics and Radioelectronics, P. Browka 6, 220013 Minsk, Belarus

ARTICLE INFO

Keywords:
High-DPI inkjet printhead
Piezoelectric cutter
Satellite ink droplet

ABSTRACT

High dots per inch (DPI) is the core index of inkjet printer, which is hindered by satellite ink droplet. Herein, we propose a novel high-DPI and monodisperse droplet inkjet printhead with the piezoelectric cutter. The as-established model has optimized the inkjet printhead structural parameters, actuating and cutting signal waveforms. The cutter element achieves moving the break-up point to the middle of the ink column, reducing the length of tail and generating a monodisperse droplet. Additionally, the cutter consistently reduces the droplet length with different ink properties including viscosity, density, surface tension, and contact angle, exhibiting high applicability. The research results provide an in-depth study on the design of high-DPI and monodisperse inkjet printheads, offering an efficient approach to improve inkjet printhead performance.

1. Introduction

Inkjet printing invented in 1858, is a digital printing technology by depositing ink droplets onto a moving substrate [1]. It has a rapid development in recent decades attributing to the advantages such as low cost, high printing quality and digital control, which is an extensively versatile technology applying for printing complex and exquisite patterns [2–4], fabricating electronic devices [5,6], producing functional materials [7,8], printing biological applications [9,10], and so on. Elegant approaches to improving the printing resolution have been developed by inkjet printing, including piezoelectric inkjet (PIJ), thermal inkjet, electrohydrodynamic inkjet, and surface acoustic-wave printing [11]. Among these, PIJ printing is the most mature and commonly used technology with merits of rapid dynamic response, convenient control, simple structure, and no heating [12].

In PIJ printing technology, the piezoelectric inkjet printhead is a crucial component for achieving high printing resolution, measured in dots per inch (DPI) [13], which has attracted considerable attention from researchers. Printheads with the resolution from 50 to 1200 DPI have been developed by researchers and companies, dramatically enhancing applications in various fields [14–18]. However, satellite droplet has long posed a challenge in improving printing DPI, as they increase the inkblot range. [19,20]. Adjusting the ink properties and driving signal waveform are the most commonly reported method for eliminating satellite droplet [21]. Critical parameters such as Reynolds number, Weber number, and Ohnesorge number describe the conditions for droplet formation [22]. By optimizing ink properties like density, viscosity, and surface tension, monodisperse droplets can be achieved. Nevertheless, the stringent requirements for usable ink properties limit applications outside of document printing [23,24]. Additionally, various actuation waveforms, including single-polar, double-polar, M-shape, and W-shape trapezoidal [15,25,26], have been developed to eliminate satellite droplets by fine-tuning their parameters. However, the increased length of waveform periods due to these complex designs hampers improvements in print speed [27]. Therefore, to broaden the range of usable ink properties and simplify waveform design, novel structures that enable monodisperse droplet printing are needed.

In this work, we present a high-DPI and monodisperse droplet inkjet

* Corresponding authors.
E-mail addresses: liucr@hdu.edu.cn (C. Liu), donglinxi@hdu.edu.cn (L. Dong), wangxiaoyuan@zjemc.org.cn (X. Wang), gaofeng@hdu.edu.cn (G. Wang).

https://doi.org/10.1016/j.jmapro.2024.07.029
Received 28 February 2024; Received in revised form 2 July 2024; Accepted 3 July 2024

printhead with a piezoelectric cutter to suppress the formation of satellite ink droplets and enhance printing resolution. Unlike traditional break-up models, the proposed PIJ printhead employs a piezoelectric cutter to apply transversal pressure, facilitating droplet breakup. The as established printhead is modeled on COMSOL Multiphysics to optimize the structural parameters and the input signal waveforms. With the optimal parameters, the cutter effectively prevents satellite droplet formation, reducing droplet length by 20 %. Furthermore, the printhead demonstrates high applicability with various ink properties, underscoring the superior performance of this high-DPI, monodisperse droplet inkjet printhead featuring a piezoelectric cutter.

2. Method

2.1. Structure design

Traditional PIJ printing modes include squeeze [28], shear [29], bend [30], and push [31]. We have designed a bend-mode PIJ printhead structure, as shown in Fig. 1. The inkjet paths are tightly arranged to achieve high DPI. Each inkjet path comprises an ink supply channel, piezoelectric actuator, piezoelectric cutter, restrictor, ink chamber, nozzle, and throat. Among these components, the piezoelectric actuator and cutter serve as driving elements based on the reverse piezoelectric effect. The actuator generates pressure to form ink droplets, while the cutter eliminates satellite droplets.

Traditional PIJ printhead utilizes an actuator to generate an ink column outside the nozzle, which breaks into a droplet with a long tail. Due to the instability associated with increased length, this process naturally results in the formation of a main droplet and several satellite droplets. The presence of satellite droplets reduces the printing DPI by extending the inkblot on the moving substrate. The variation ratio (δ) is described as:

$$\delta = \frac{D_m}{D_m + \sum_i \left(D_s^i + l^i\right)} \tag{1}$$

where D_m is diameter of main droplet, $Di\ s$ is diameter of the num. i satellite droplet, and l^i is the interval between the num. i satellite droplet and num. (i - 1) droplet (num. 0 remarks the main droplet). Here, we designed a piezoelectric cutter to reduce the length of ink blot by promoting the break-up of the ink column.

This design integrates the driving forces of the piezoelectric actuator and cutter, utilizing the d_{33} and d_{31} [32,33] deformations (Fig. S1), respectively. The cutter element is installed beneath the nozzle plate as shown in Fig. 1, replacing part of the throat and controlling the formation of the ink column. When an ink column gradually forms under the driving force of the actuator, an electric field is applied to the piezoelectric cutter. The cutter induces a transversal deformation, resulting in the reduction of the throat diameter. This variation generates an inward pressure wave within the ink column, accelerating its necking process. Subsequently, the cutter recovers when the electric field is removed, slowing down the ink flow. The cutter's deformation and recovery operate together to create a new break-up position in the middle of the ink column. Consequently, the droplet length is reduced due to the cutting effect, improving stability and preventing the generation of satellite droplets. The resulting monodisperse droplet leaves a shorter inkblot on the substrate, thereby enhancing printing precision.

2.2. Modeling

The optimization and analysis of novel printhead are numerically simulated using COMSOL Multiphysics. To enhance the simulation speed and accuracy, the printhead model is divided into four parts: the piezoelectric actuator model, the printhead model, the piezoelectric cutter model, and the inkjet model, as illustrated in Fig. 2. The boundary

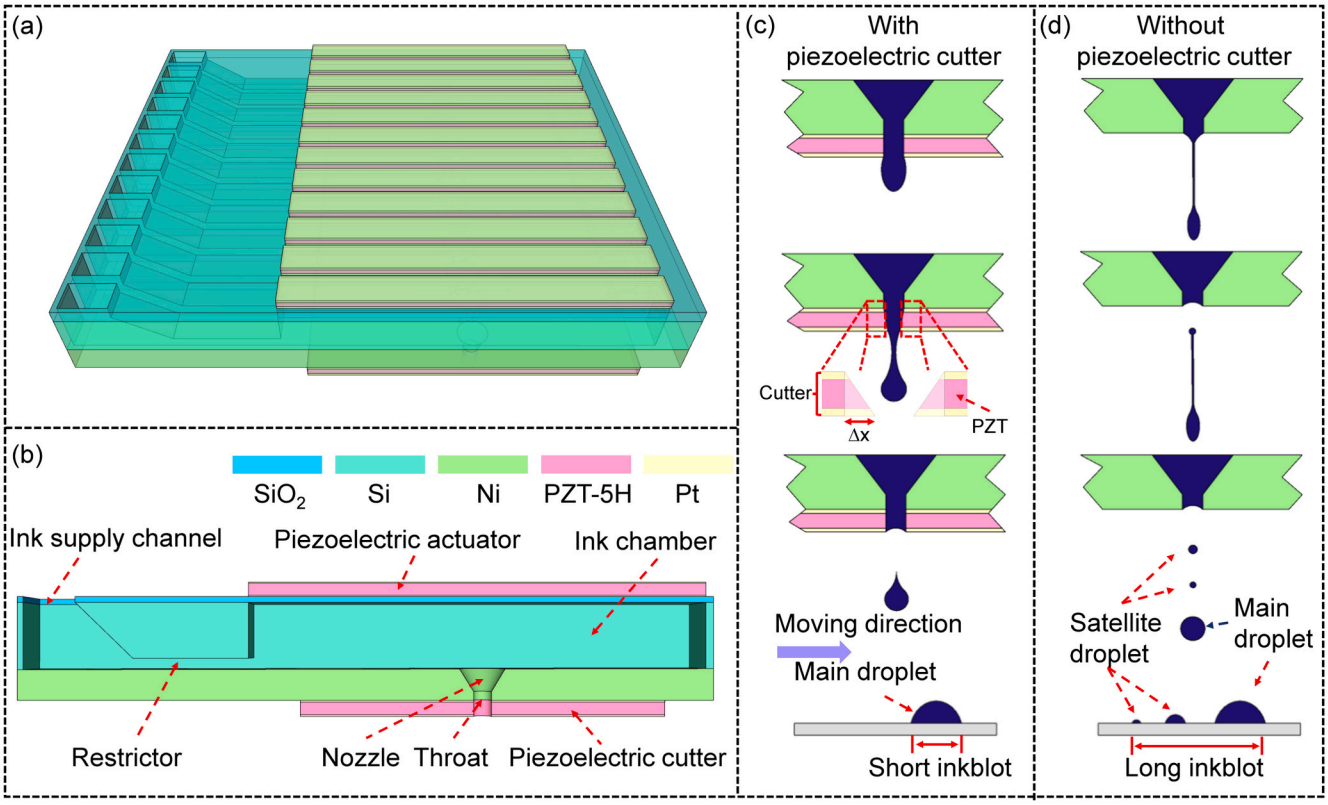

Fig. 1. Schematic of the novel high-DPI and monodisperse droplet inkjet printhead with the piezoelectric cutter. (a) Structure of arranged high-DPI PIJ printhead. (b) Cross-section drawn of single PIJ printhead. Schematic of ink ejection (c) with piezoelectric cutter, (d) without piezoelectric cutter.

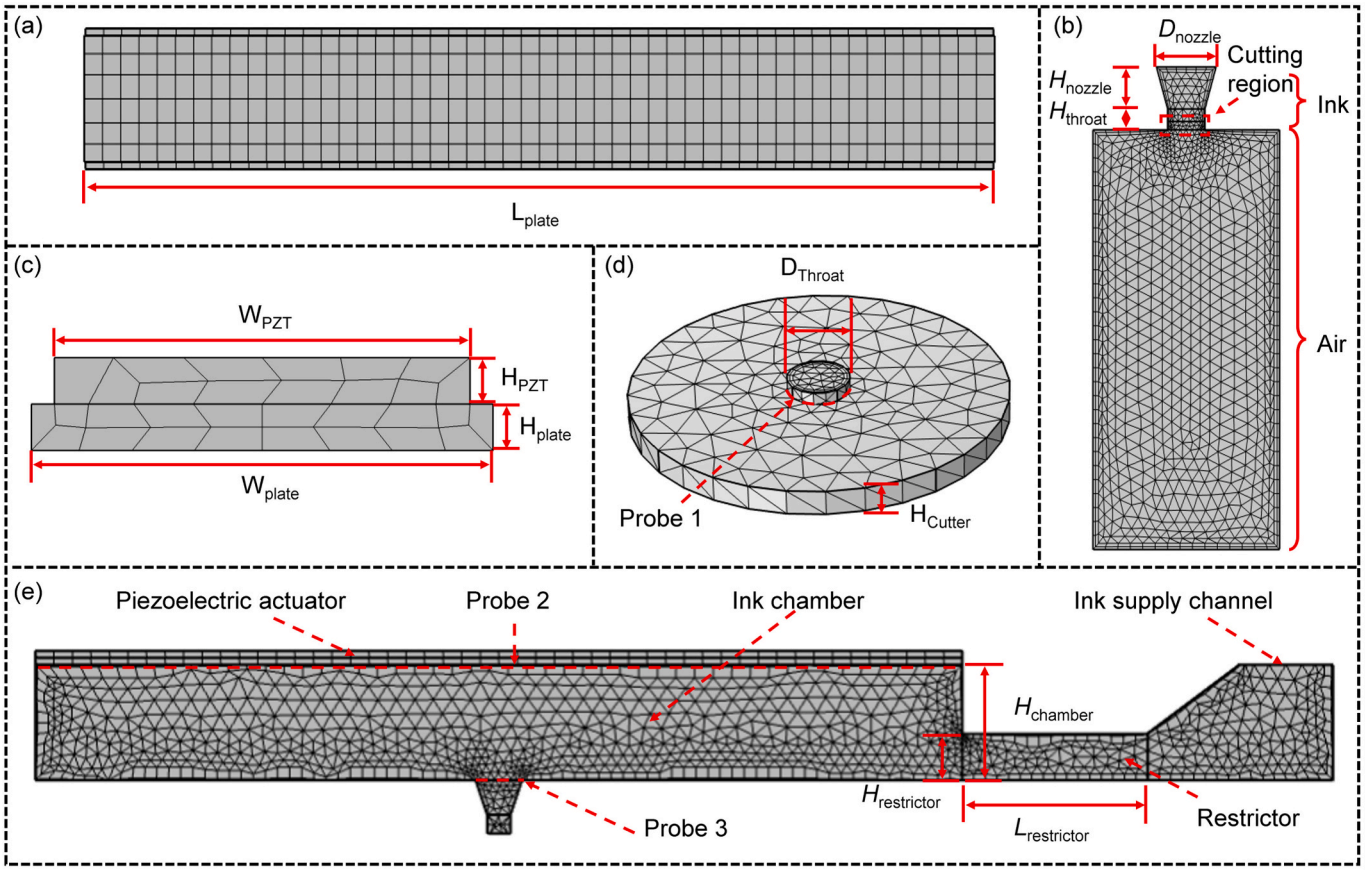

Fig. 2. The as established printhead simulation models. (a) Piezoelectric actuator model (Top view). (b) Inkjet model. (c) Piezoelectric actuator model (side view). (d) Piezoelectric cutter model. (e) Printhead model.

settings of these models are detailed in the supporting materials.

The actuator model comprises the piezo domain and the SiO_2 vibration plate domain, with its top and side views depicted in Fig. 2 (a) and (c), respectively. This model is based on piezoelectricity, which is described by the following equation[34]:

$$[D_i] = \left[\varepsilon_{ij}^{T}\right][E_j] + [d_{il}][T_l] \tag{2}$$

$$[S_k] = [d_{jk}]^{T}[E_j] + [s_{kl}^{E}][T_l] \tag{3}$$

where $[D_i]$ is electric displacement vector, $[\varepsilon_{ij}]$ is dielectric constant matrix, $[E_j]$ is electric intensity vector, $[d_{il}]$ is piezoelectric coefficient tensor, $[T_l]$ is stress vector, $[S_k]$ is strain vector, $[s_{kl}]$ is elastic flexibility tensor. The deformation mechanism of a piezo material with pole direction of third coordinate axis (y-axis) is shown in Fig. S1. Its piezoelectric coefficient tensor can be described as:

$$[d] = \begin{bmatrix} & & & d_{15} & \\ & & & & d_{15} \\ d_{31} & d_{31} & d_{33} & & \end{bmatrix} \tag{4}$$

When an electric field parallel to poling direction is applied to the material, it induces longitudinal, transversal, and shear strain derived from piezoelectric coefficient d_{33}, d_{31}, and d_{15}. In our design, the d_{33} and d_{31} deformation is employed as the driving forces in inkjet process, whose deformation can be calculated by [20]:

$$\frac{\Delta y}{h} = \frac{d_{33}U}{h} \tag{5}$$

$$\frac{\Delta x}{l} = \frac{d_{31}U}{h} \tag{6}$$

where Δy is the deformation in 3-direction, Δx is the deformation in 1 and 2 direction, U is the voltage, h is the thickness of material, l is the length of material. In the printhead design, PZT-5H is chosen as the piezo material due to its excellent sensitivity and dielectric constant, with the piezoelectric coefficient value are: $d_{31} = -2.74 \times 10^{-10}$C/N, $d_{33} = -5.93 \times 10^{-10}$C/N, and $d_{15} = -7.41 \times 10^{-10}$C/N.

The printhead model is constructed based on the coupling of piezoelectricity and fluid-solid interaction, encompassing the piezoelectric actuator domain and the inkjet printing path domain (model dimensions are provided in Table S1). Due to the extensive contact interface between the solid and liquid components, the force exerted by the ink cannot be ignored. Consequently, the interaction between the ink and the actuator is set as a bidirectional coupling. The fluid-solid interaction including the equation of fluid flow, structure deformation, and boundary interaction. The initial ink density and viscosity are 1050 kg/m^3 and 10 mPa·s respectively. Thus, the ink flow can be considered laminar, as determined by the Reynolds number [35]:

$$Re = \frac{\rho_{\text{fluid}}\overline{u}_{\text{fluid}}L_{\text{plate}}}{\mu} \tag{7}$$

where ρ_{fluid} represents the fluid density, $\overline{u}_{\text{fluid}}$ is the fluid velocity norm, L_{plate} is the ink chamber length, and μ is the fluid viscosity coefficient. It is noted that there is no heat transfer in the printing process, thus the ink flow can be calculated by the governing equations of continuity equation and Navier-Stokes Eq. [36]. The continuity equation comes from the mass conservation of infinitary:

$$\frac{\partial \rho_{\text{fluid}}}{\partial t} + \nabla\cdot\left(\rho_{\text{fluid}}\mathbf{u}_{\text{fluid}}\right) = 0 \tag{8}$$

where t is time, $\mathbf{u}_{\text{fluid}}$ is the fluid velocity vector. The Navier-Stokes equation comes from the momentum conservation of Newton's second law:

$$\rho_{\text{fluid}}\left(\frac{\partial \mathbf{u}_{\text{fluid}}}{\partial t}+\mathbf{u}_{\text{fluid}}\cdot\nabla\mathbf{u}_{\text{fluid}}\right)=\mathbf{f}+\nabla\cdot\mathbf{T} \tag{9}$$

where $\mathbf{f}$ is the external forces, and $\mathbf{T}$ is the stress tensor. Additionally, the structure deformation is described by the governing equation:

$$\rho_{\text{solid}}\frac{\partial^2\mathbf{u}_{\text{solid}}}{\partial t^2}-\nabla\cdot\sigma=\mathbf{F} \tag{10}$$

where $\mathbf{F}$ is the volume force, σ is stress tensor, ρ_{solid} is the fluid density, and $\mathbf{u}_{\text{solid}}$ is the fluid velocity vector. The bidirectional coupling fluid-solid interaction boundary is described by [37]:

$$\mathbf{u}_{\text{fluid}}=\mathbf{u}_{\text{w}}=\frac{\partial \mathbf{u}_{\text{solid}}}{\partial t} \tag{11}$$

$$\sigma\cdot\mathbf{n}=\mathbf{T}\cdot\mathbf{n} \tag{12}$$

where $\mathbf{u}_{\text{w}}$ is the fluid velocity at the boundary, $\mathbf{n}$ is boundary normal vector.

It models the piezoelectric cutter model based on the coupling of piezoelectricity and fluid-solid interaction, comprising the cutter domain and ink domain. This model analyzes the deformation of the cutter with a thickness of 2 μm and a diameter of 30 μm. Compared with the deformation driven by electric field, the cutter deformation induced by high-speed ink flow can be neglected due to the high radial depth, indicating an obvious unidirectional coupling from solid to liquid. Thus, the deformation of piezoelectric cutter can be the prescribed mesh displacement in the inkjet model.

The inkjet model is based on the two-phase flow (level-set method), consisting of the ink domain and air domain. The lower part of the throat slides to the cutter region, utilizing prescribed mesh displacement to simplify the computation in solid-liquid interaction. Additionally, the level set method is a reinitialized and conservative approach to describe and track the fluid interface. The 0.5 contour of the level set function ϕ defines the interface, ϕ equals 0 in air and 1 in ink. In a transition layer close to the interface, ϕ smoothly transitions from 0 to 1. The convection of the reinitialized level set function can be described as [38]:

$$\frac{\partial\phi}{\partial t}+\mathbf{u}_{\text{fluid}}\cdot\nabla\phi+\omega\left[\left(\nabla\cdot\left(\phi(1-\phi)\frac{\nabla\phi}{|\nabla\phi|}\right)\right)-\varepsilon\nabla\cdot\nabla\phi\right]=0 \tag{13}$$

where ε is proportional to the thickness of the transition layer, and ω determines the amount of reinitialization.

3. Result

3.1. Printing process analysis

The piezoelectric cutter demonstrates its effectiveness in eliminating satellite droplets, as shown in Fig. 3 and Video S1. Traditional printheads utilize a piezoelectric actuator to promote droplet formation, without the cutter. The actuator induces pressure waves in the ink chamber and generates a long ink column at the nozzle. As the column gradually elongates, its thinnest position (also known as the neck) appears near the nozzle, where breakup occurs to form a droplet. This

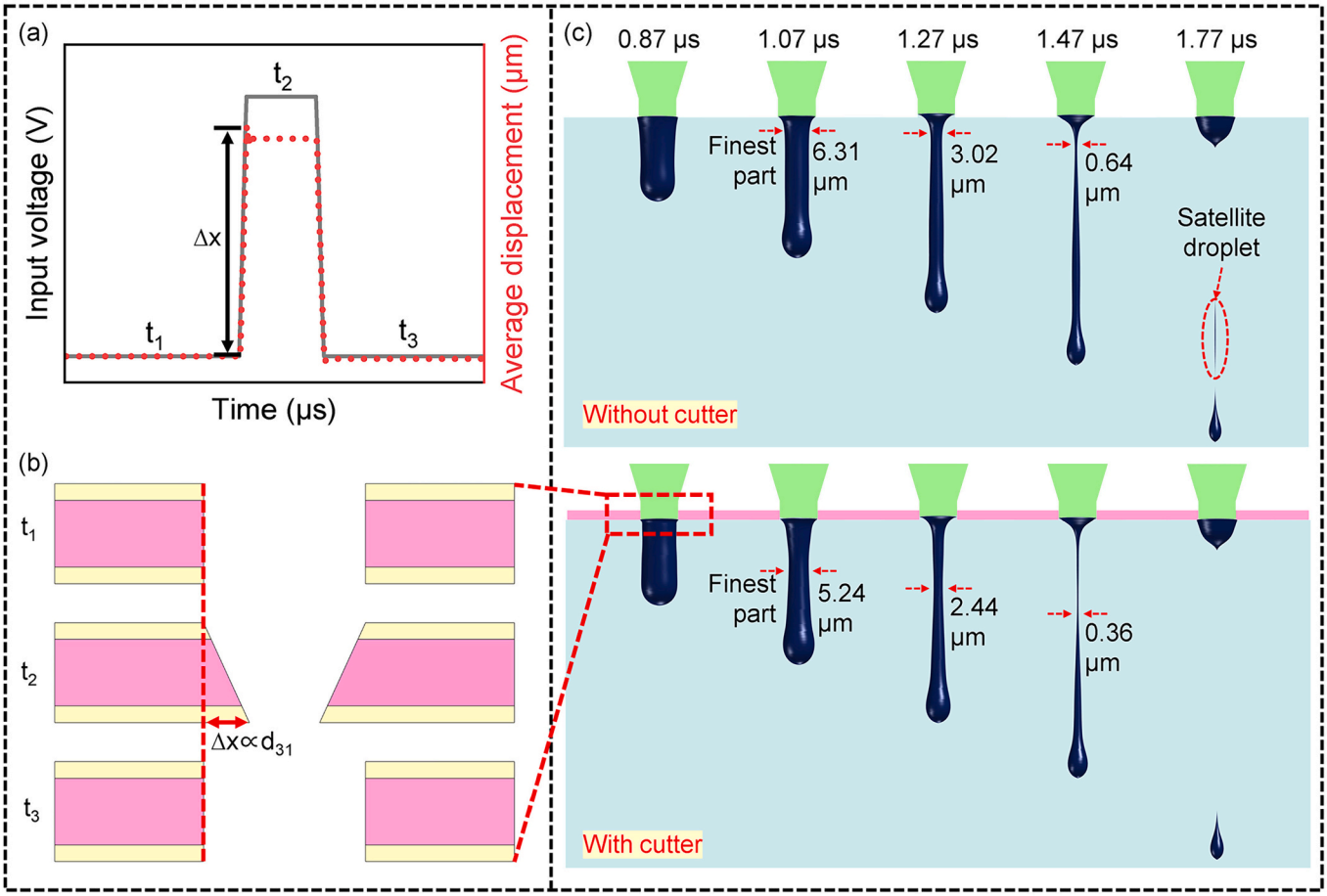

Fig. 3. The inkjet process of the as designed printhead. (a) Input cutting signal and cutter's deformation curve. (b) The states of cutter during different time. (c) Inkjet process with and without the piezoelectric cutter.

droplet typically has a long tail, increasing its overall length. The extended length of the droplet contributes to the formation of satellite droplets, causing the droplet to become unstable and undergo a subsequent secondary breakup.

Nevertheless, a monodisperse droplet is ultimately generated when employing the piezoelectric cutter under the same condition. The printing process of the novel printhead relies on the synergistic action of actuator and cutter. The deformation of actuator induces the velocity variation in the ink chamber, pushing ink out of the nozzle and forming an ink column. Whereafter, the cutter deforms lagging behind the peak value of the ink column velocity, generating the velocity variation twice, as shown in Fig. S3. This creates a neck in the middle of the ink column, which becomes thinner over time. Notably, the deformation of the cutter begins after the actuator stops working, avoiding complicated interaction. As the neck of the ink column elongates, it exhibits a thinner profile compared to scenarios without the cutter. Eventually, the ink column breaks to form a droplet with a shorter length, enhancing stability and eliminating the possibility of generating satellite droplets.

3.2. Optimizing of actuator parameters

Numerical simulations are carried out to achieve high DPI printing, involving the structural parameters optimization, signal waveforms design, and ink ejection process comparison. Sufficient actuating pressure is necessary for forming an ink droplet. The structural optimization results (Fig. S4) indicate that a thinner PZT and SiO_2 plate provides more driving force in printing. However, a narrower actuator faces challenges in deformation due to increased material stiffness, resulting in insufficient driving power. Notably, the actuator deformation curves reveal the presence of residual vibrations that affect the actuator's deformation process, delaying subsequent variations. Here, an actuator with a 20 μm width is chosen to achieve high DPI printing, and the actuating signal waveform is optimized to provide higher ink flow velocity.

The trapezoidal signal waveform is commonly used in PIJ printheads and consists of four key parameters (Fig. 4a): the time of the voltage rising section (t_r), the time of the voltage dwelling section (t_d), the time of the voltage falling section (t_f), and the amplitude (U). Simulation results in Fig. 4b-c indicate that shorter actuator rising and falling times result in higher amplitude pressure waves in the ink flow. Moreover, when the dwelling time is shorter than the period of one pressure wave's propagation (t_p) (as defined in Eq. S2), interactions between pressure waves occur, leading to variations in ink flow velocity.

Therefore, the parameters are further optimized to enhance the actuating force through the utilization of pressure waves (Fig. 4 e-g). The maximum ink flow velocity is relative improved at $t_{r\text{-actuator}} = 0.2$ and 0.4 μs, signifying the accumulation of the pressure wave generated during the falling time with the residual one. Here, the rising time of 0.2 μs is selected due to the higher ink flow velocity. Similarly, maximum velocities are observed at $t_{d\text{-actuator}} = 0.2$ μs and $t_{f\text{-actuator}} = 0.2$ μs, showcasing optimal accumulation of the two pressure waves. The relationship between actuator deformation and ink flow velocity in Fig. 4h suggests that the actuator's recovery should commence at half the wavelength of ink flow. Due to the residual vibration of actuator, the recovery of actuator is delayed compared to the falling part of the signal. Therefore, the waveform parameters should meet the requirement of $t_{r\text{-actuator}} + t_{d\text{-actuator}} < t_p/2$ to ensure optimal performance. Meanwhile, the falling time $t_{f\text{-actuator}} = t_p/4$ controls the amplitude and lasting time of the pressure wave, which is induced by the recovery of actuator.

We have explored the impact of input signal amplitude and ink properties in Fig. S5. The finding reveals that the signal amplitude is directly proportional to the maximum velocity, while increasing ink viscosity and density decelerate the ink flow. Additionally, various ink viscosities exhibit identical t_p values, whereas ink density influences the propagation of the pressure wave. This suggests that signal waveforms should be adjusted according to different ink densities to better utilize the actuating forces in printing.

3.3. Optimizing and characteristic of cutter

The droplet length is a significant factor contributing to the formation of satellite droplets, as a long tail breaks up easily due to its instability. Therefore, to decrease the droplet length, cutting signal waveform parameters are optimized through simulation (Fig. 5), including the cutter waveform dwelling time ($t_{d\text{-cut}}$), waveform starting time ($t_{s\text{-cut}}$), and deformation amplitude (D_{cut}). The simulations are conducted with the ink properties set at a viscosity of 10 mPa·s, density of 1050 kg/m^3, and surface tension of 0.07 N/m^2. Besides, the rising and falling time are set at 0.01 μs to provide higher cutting pressure, and the deformation displacement of cutter is acquired through the piezoelectric cutter model (Fig. S6).

Droplet length is reduced with a shorter $t_{d\text{-cut}}$ value compared to the sceneries without the cutter. The less dwelling time shorten the interval between the cutter's deformation and recovery, concentrating the contribution of cutter pressure, which results in the necking of ink column. Consequently, the column breaks to form a shorter droplet, with the minimum length observed when $t_{d\text{-cut}} = 0.1$ μs. Then, ejection with smaller $t_{s\text{-cut}}$ value generates a droplet with a decreased length, as the earlier cutting moves the break-up point downwards. It is noted that the cutting should start after the maximum ink flow velocity to avoid hindering the ink column formation. Finally, the increasing deformation amplitude of cutter provides more pressure on the ink column, and the thoroughly slicing is occurred when $D_{cut} = 0.45$ μm. According to the results, the cutter achieves a monodisperse droplet with the shortest tail length (reduced by 20 %) when parameters are set to $t_{d\text{-cut}} = 0.10$ μs, $t_{s\text{-cut}} = 0.75$ μs, and $D_{cut} = 0.45$ μm.

To verify the applicability, the cutter structure is operated under various ink properties (viscosity, density, surface tension, and contact angle). The simulation results in Fig. 6 depict that satellite droplets are easily generated in the absence of the cutter. An elongated tail forms during ink ejection, left at the nozzle when the ink viscosity is <6 mPa·s. Meanwhile, the higher viscosity ink generates long droplet. Both of them are unstable due to the long length, which is easily broken, leading to the formation of satellite droplets. Additionally, higher ink density tends to increase the droplet length, augmenting the likelihood of satellite droplets formation.

Nevertheless, the droplet break-up points consistently move to the middle when the cutter is employed, irrespective of variations in ink viscosity and density. The generated tail (viscosity <6 mPa·s) and droplet (viscosity ≥6 mPa·s) are both short due to the cutting effect. Particularly, the cutter reduces the droplet length by 31 % at an ink viscosity of 8 mPa·s. Thus, the stability is enhanced with the shortened length, resulting in the formation of monodisperse droplet. Similarly, the cutter slices the ink column with different ink density, lead to a reduction in droplet length, which significantly avoids the generation of satellite droplet. Additionally, the piezoelectric cutter performs excellently with different ink surface tension and contact angle (Fig. S7–8), shortening the droplet length compared to the ejection result without the cutter. Subsequently, no satellite droplet is created attributing to the enhanced stability of the droplet. Hence, the results demonstrate that the cutter structure addresses the challenge of generating satellite droplets by shortening the droplet length, which improves the printing precision with various ink properties.

4. Discussion

There are two modes of satellite droplet generation: multiple breakup due to capillary waves and end-pinching where pinch off from the thread and head. These modes are influenced by the combined effects of the Ohnesorge number, thread length, and capillary wavelength [39]. In this study, the droplet completely breaks in the end-pinching mode, whether it is the first breakup or secondary breakup. The capillary wave does not appear with the movement of the droplet, and necking mainly results in the end-pinching mode. During the inkjet

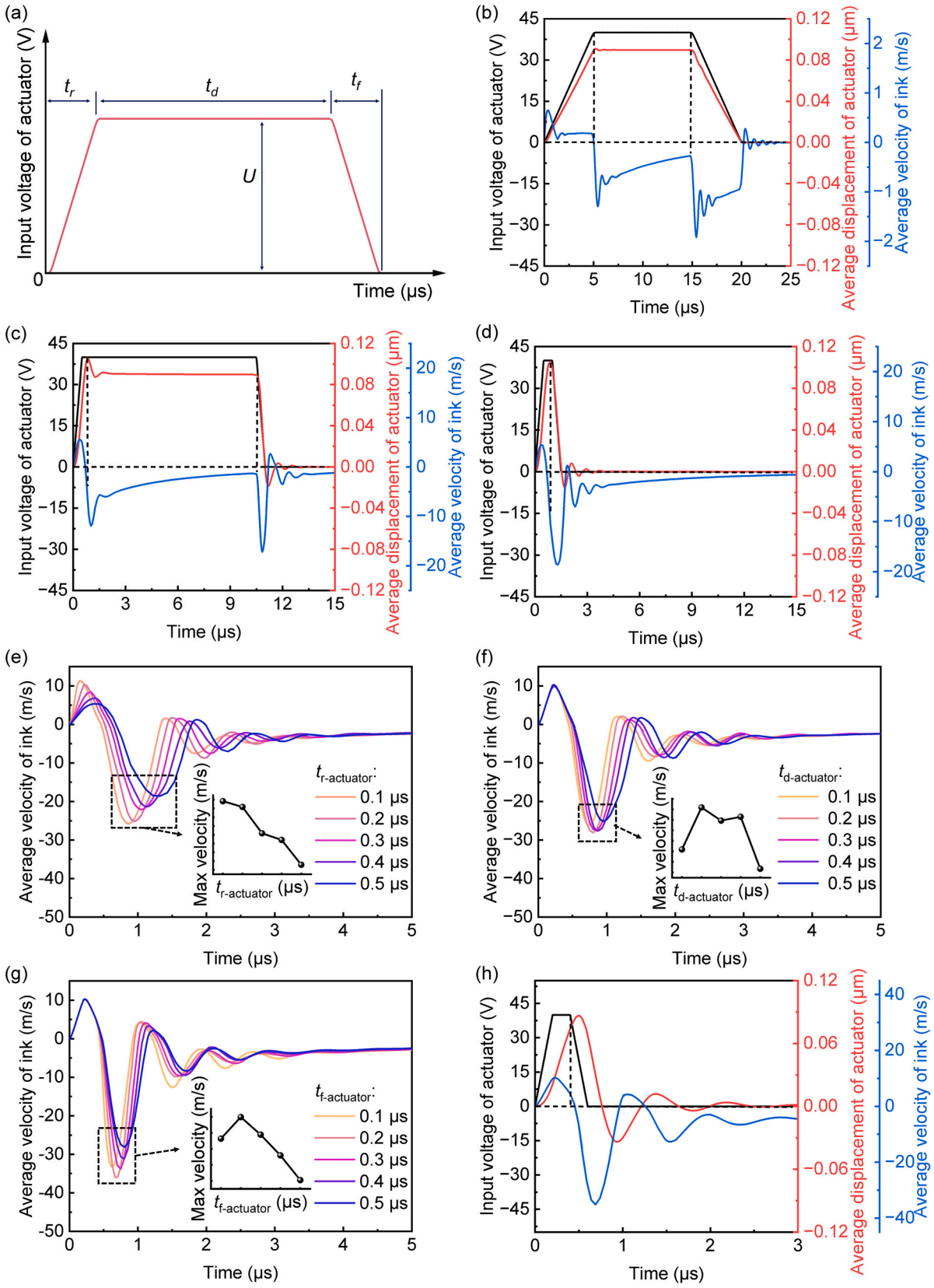

Fig. 4. Results of actuating signal waveform optimizing. (a) Parameters of driving signal waveform. Average deformation and velocity curves when the parameters are set to (b) $t_{r\text{-actuator}} = 5$ μs, $t_{d\text{-actuator}} = 10$ μs, and $t_{f\text{-actuator}} = 5$ μs, (c) $t_{r\text{-actuator}} = 0.5$ μs, $t_{d\text{-actuator}} = 10$ μs, and $t_{f\text{-actuator}} = 0.5$ μs, (d) $t_{r\text{-actuator}} = 0.5$ μs, $t_{d\text{-actuator}} = 0.5$ μs, and $t_{f\text{-actuator}} = 0.5$ μs. Average velocity curves with different (e) $t_{r\text{-actuator}}$ at $t_{d\text{-actuator}} = 0.5$ μs, $t_{f\text{ -actuator}} = 0.5$ μs, (f) $t_{d\text{-actuator}}$ at $t_{r\text{-actuator}} = 0.2$ μs, $t_{f\text{-actuator}} = 0.5$ μs, (g) $t_{f\text{-actuator}}$ at $t_{r\text{-actuator}} = 0.2$ μs, $t_{f\text{-actuator}} = 0.2$ μs. (h) With the optimized signal, the curves of average velocity of ink, average displacement of actuator, and input signal.

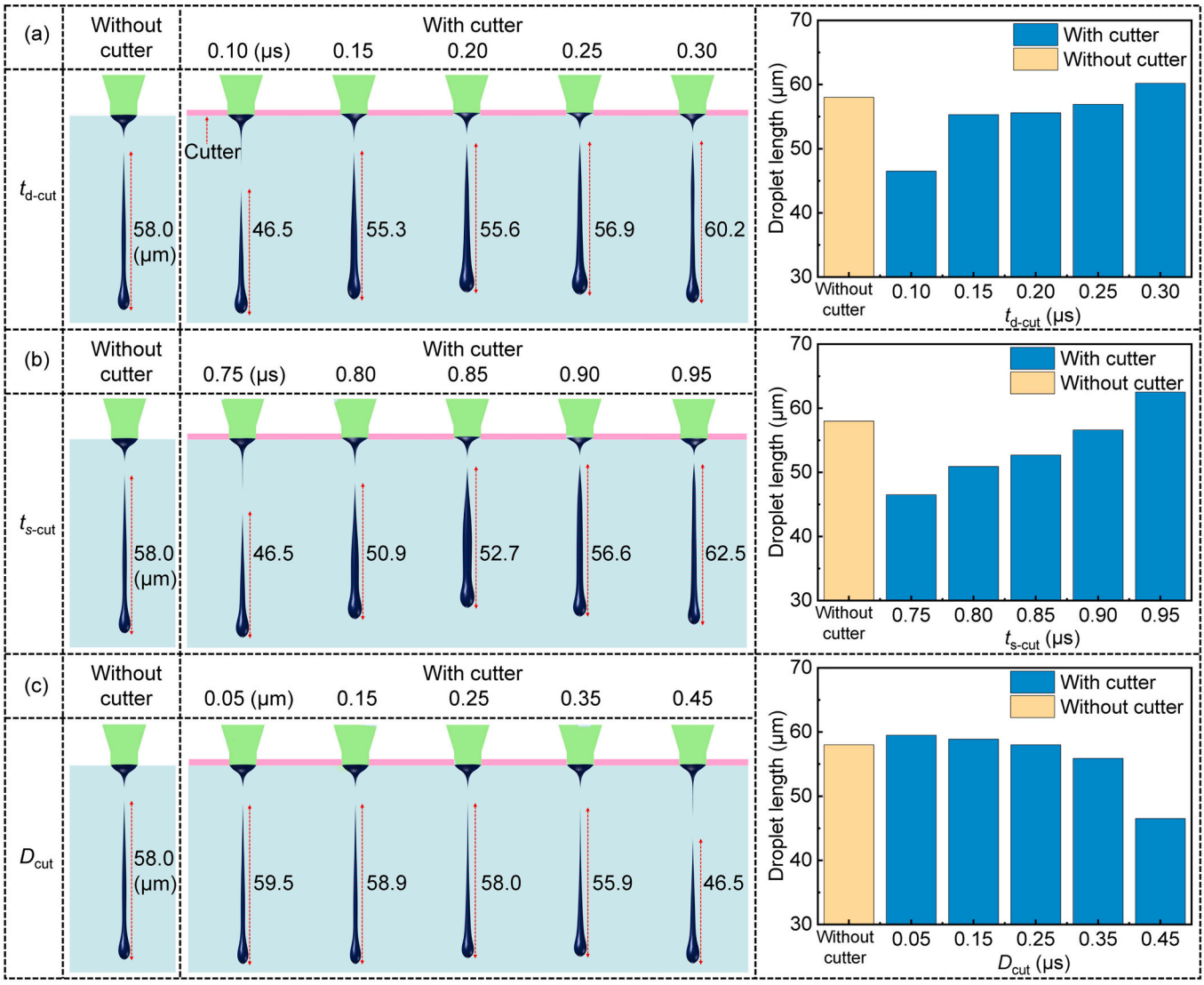

Fig. 5. Ink ejection results with different cutter deforming parameters. The simulation results and droplet length comparison with different (a) dwelling time ($t_{d\text{-}cut}$), (b) starting time ($t_{s\text{-}cut}$), (c) deformation amplitude (D_{cut}).

process, the ink column has a continuous centripetal velocity driven by the transversal pressure of cutter deformation. Similarly, the recovery of the cutter generates an inverse centripetal velocity, which drags the upper part of the ink column. The transversal velocity variation of the ink column forms a neck in the middle of it. It is noted that the variation propagates in the form of a pressure wave, which is the same as in the ink chamber. As the ink column elongates, the neck will move down, remaining in the middle position throughout. Subsequently, the ink column breaks up from the neck, pinching off a considerable length compared to without the cutter.

Hongming Dong [39] has deduced the condition of eliminating satellite droplet in end-pinching mode. The droplet contracts into a single drop without breaking up with its length less than a limiting value l^* b, which can be described as:

$$l_b^* = \left(\frac{A(t_{b1} - t_{b2})}{t_{ca}} + 2\right) R_{nozzle} \tag{14}$$

where R_{nozzle} is the nozzle radios, A is a constant calculated in experiment, t_{b1} is the first breakup time from nozzle, t_{b2} is the secondary breakup time of generating satellite droplet, $t_{ca} = (\rho R3\ \text{nozzle}/\mu)^{1/2}$ is the capillary time. Hence, the droplet length is critical to judge if satellite droplet will be generated, which has been reported by Pimbley [40]:

$$l_b^A = -\frac{\overline{u}_{liquid}}{\gamma} log\left(\frac{\pi \Delta \overline{u}_{liquid}}{2\lambda\gamma}\right) \tag{15}$$

where $\Delta\overline{u}_{liquid}$ is the velocity disturbance amplitude, λ is the instability wavelength, and γ is instability growth rate, which can be calculated by:

$$t_{ca}\gamma = \sqrt{\frac{1}{2}(x^2 - x^4) + \frac{9}{4}Oh^2x} - \frac{3}{2}Ohx^2 \tag{16}$$

where x is the dimensionless wave number. The breakup length is further corrected by Pimbley and Lee [40] which is defined as:

$$l_b = l_b^A + l^D - l^C \tag{17}$$

where l^D is diffusive length described as:

$$l^D = \frac{\rho_{fluid}}{\mu} \int_S |u_z - \overline{u}_{liquid}| dS \tag{18}$$

and l^C is convective length described as:

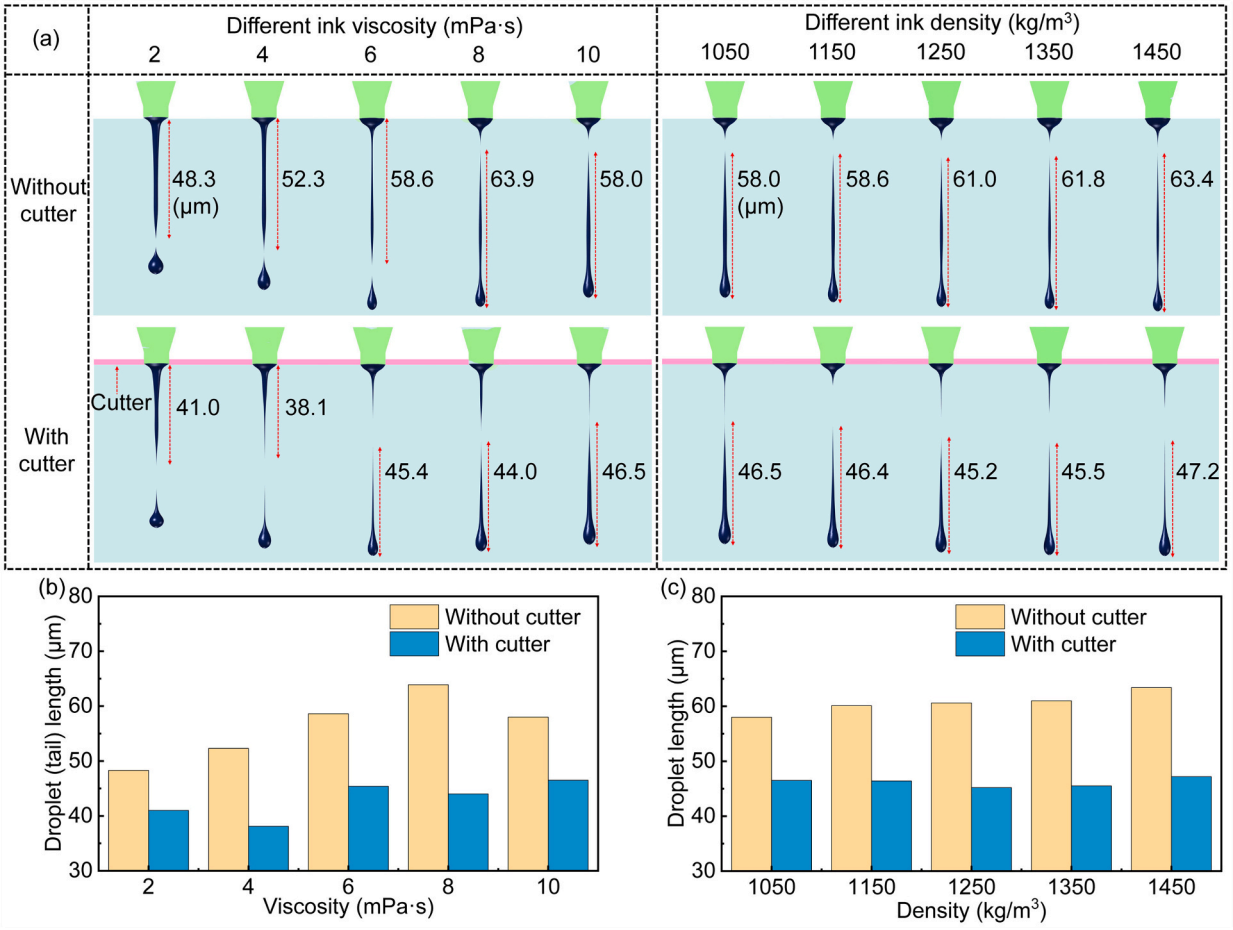

Fig. 6. Simulation results at different ink viscosity and density. (a) The formed droplet at different viscosity and density. (b) The length comparison between without and with the cutter at different ink viscosity. (c) The length comparison between without and with cutter at different ink density.

$$l^C = \pi \frac{\rho_{\text{fluid}}}{\gamma} \int_S |u_r u_z| dS \tag{19}$$

where S is the profile section, u_r and u_z are the radial and axial component of velocity vector.

By introducing the pinch-off length through the piezoelectric cutter, the droplet length can be reduced to a value less than $l^* b$. Consequently, the droplet contracts into a single drop, eliminating satellite droplets. To integrate the cutter element into a commercial printhead, its cutting waveform should be adjusted according to the optimization of the cutter. The deformation and recovery interval $t_{\text{d-cut}}$ should be short enough; otherwise, two necks will be induced. Having more necks weakens the effect of the cutter, decreasing the reduction of droplet length. The cutter deformation should slightly lag behind the maximum velocity of ink flow to ensure the neck position appears in the middle of the ink column. Moreover, the cutter is required to provide sufficient driving forces, which can be approached by improving the deformation velocity and displacement.

5. Conclusion

In summary, this paper designs a novel high-DPI and monodisperse droplet inkjet printhead model, providing a waveform optimizing method and achieving the absence of satellite droplet formation with the piezoelectric cutter. Superposition of pressure waves is enabled to improve the ink velocity, when the actuator's recovery starts at half the wavelength of ink flow ($t_{\text{r-actuator}} + t_{\text{d-actuator}} < t_p/2$ and $t_{\text{f-actuator}} = t_p/4$). The piezoelectric cutter shortens the droplet length by 20 % at the parameters of $t_{\text{d-cut}} = 0.1$ μs, $t_{\text{s-cut}} = 0.75$ μs, and $D_{\text{cut}} = 0.45$ μm. Additionally, the novel structure is highly applicable to various ink properties, including viscosity, density, surface tension, and contact angle. The designed printhead consistently eliminates the satellite droplet due to the high stability of short droplet, significantly improving the printing precision. This technology holds the potential for designing higher-DPI printheads and applications in a broader range of fields.

Supplementary data to this article can be found online at https://doi.org/10.1016/j.jmapro.2024.07.029.

CRediT authorship contribution statement

Xucong Wang: Writing – original draft, Methodology. **Chaoran Liu:** Writing – review & editing, Writing – original draft. **Defei Yao:** Methodology. **Hongjian Lin:** Methodology. **Jing Yu:** Methodology. **Xin Tong:** Validation. **Zai Wang:** Validation. **Yi Wang:** Validation. **Weihuang Yang:** Validation. **Yu Gao:** Investigation. **Serguei Lazarouk:** Investigation. **Vladimir Labunov:** Investigation. **Linxi Dong:** Supervision, Funding acquisition. **Xiaoyuan Wang:** Supervision, Funding acquisition. **Gaofeng Wang:** Supervision, Funding acquisition.

Declaration of competing interest

The authors declare that they have no known competing financial interests or personal relationships that could have appeared to influence the work reported in this paper.

Acknowledgements

This work was supported by the National Key R&D Program of China (No. 2022YFB3204800) and the Open Funding of Zhejiang Key Laboratory of Ecological and Environmental Big Data (No. EEBD-2022-02).

References

[1] Singh M, Haverinen HM, Dhagat P, Jabbour GE. Inkjet printing-process and its applications. Adv Mater 2010;22:673–85. https://doi.org/10.1002/adma.200901141.
[2] Wu Y, Ren J, Zhang S, Wu S. Nanosphere-aggregation-induced reflection and its application in large-area and high-precision panchromatic inkjet printing. ACS Appl Mater Interfaces 2020;12:10867–74. https://doi.org/10.1021/acsami.0c00547.
[3] Wang Y, Chen J, Yin Z, Li Y. A high-adaptability nozzle-array printing system based on a set covering printing planning model for printed display manufacturing. Sci Rep 2023;13:156. https://doi.org/10.1038/s41598-022-24135-3.
[4] G.D. Martin, M. Willis, Inkjet technology: what next?, Fundamentals of inkjet printing: the science of inkjet and droplets 2015, pp. 419–44. doi:https://doi.org/10.1002/9783527684724.ch16.
[5] Zhuo L, Liu W, Zhao Z, Yin E, Li C, Zhou L, et al. Cost-effective silver nano-ink for inkjet printing in application of flexible electronic devices. Chem Phys Lett 2020;757. https://doi.org/10.1016/j.cplett.2020.137904.
[6] Sajedi-Moghaddam A, Rahmanian E, Naseri N. Inkjet-printing technology for supercapacitor application: current state and perspectives. ACS Appl Mater Interfaces 2020;12:34487–504. https://doi.org/10.1021/acsami.0c07689.
[7] Lee SJ, Heo DN, Heo M, Noh MH, Lee D, Park SA, et al. Most simple preparation of an inkjet printing of silver nanoparticles on fibrous membrane for water purification: technological and commercial application. J Ind Eng Chem 2017;46:273–8. https://doi.org/10.1016/j.jiec.2016.10.039.
[8] Glinsek S, Song L, Kovacova V, Mahjoub MA, Godard N, Girod S, et al. Inkjet-printed piezoelectric thin films for transparent haptics. Adv Mater Technol 2022;7. https://doi.org/10.1002/admt.202200147.
[9] Zub K, Hoeppener S, Schubert US. Inkjet printing and 3D printing strategies for biosensing, analytical, and diagnostic applications. Adv Mater 2022;34:e2105015. https://doi.org/10.1002/adma.202105015.
[10] Hussain A, Abbas N, Ali A. Inkjet printing: a viable technology for biosensor fabrication. Chemosensors 2022;10. https://doi.org/10.3390/chemosensors10030103.
[11] Eshkalak SK, Chinnappan A, Jayathilaka W, Khatibzadeh M, Kowsari E, Ramakrishna S. A review on inkjet printing of CNT composites for smart applications. Appl Mater Today 2017;9:372–86. https://doi.org/10.1016/j.apmt.2017.09.003.
[12] Shah MA, Lee D-G, Lee B-Y, Hur S. Classifications and applications of inkjet printing technology: a review. IEEE Access 2021;9:140079–102. https://doi.org/10.1109/access.2021.3119219.
[13] Huckaba AJ, Lee Y, Xia R, Paek S, Bassetto VC, Oveisi E, et al. Inkjet-printed mesoporous TiO2 and perovskite layers for high efficiency perovskite solar cells. Energ Technol 2019;7:317–24. https://doi.org/10.1002/ente.201800905.
[14] Wei H, Xiao X, Yin Z, Yi M, Zou H. A waveform design method for high DPI piezoelectric inkjet print-head based on numerical simulation. Microsyst Technol 2017;23:5365–73. https://doi.org/10.1007/s00542-017-3301-4.
[15] Liu N, Sheng X, Zhang M, Han W, Wang K. Squeeze-type piezoelectric inkjet printhead actuating waveform design method based on numerical simulation and experiment. Micromachines 2022;13:1695. https://doi.org/10.3390/mi13101695.
[16] Wang S, Han X, Gao X, Zhang H, Li C, Duan S, et al. The evaluation and exploration of piezoelectric parameter optimization for droplet ejection in binder jet 3D printing drugs. 3D Printing and Additive Manufacturing 2022. https://doi.org/10.1089/3dp.2022.0131.
[17] Lei T, Han J, Liu H. Numerical analysis and optimal CFD model verification of piezoelectric inkjet Printhead. Journal of Applied Fluid Mechanics 2022;15:1087–97. https://doi.org/10.47176/jafm.15.04.33396.
[18] Murata M, Kondoh T, Yagi T, Funatsu N, Tanaka K, Tsukuni H, et al. High-resolution piezo inkjet printhead fabricated by three dimensional electrical connection method using through glass VIA. In: 2009 IEEE 22nd International Conference on Micro Electro Mechanical Systems. IEEE; 2009. p. 507–10.
[19] Wijshoff H. The dynamics of the piezo inkjet printhead operation. Phys Rep 2010;491:77–177. https://doi.org/10.1016/j.physrep.2010.03.003.
[20] Wijshoff H. Structure-and fluid-dynamics in piezo inkjet printheads. University of Twente; 2008.
[21] Li H, Liu J, Li K, Liu Y. Piezoelectric micro-jet devices: a review. Sensors Actuators A Phys 2019;297:111552. https://doi.org/10.1016/j.sna.2019.111552.
[22] Jiao T, Lian Q, Zhao T, Wang H. Influence of ink properties and voltage parameters on piezoelectric inkjet droplet formation. Applied Physics A 2021;127:1–9. https://doi.org/10.1007/s00339-020-04151-8.
[23] Yang Q, Li H, Li M, Li Y, Chen S, Bao B, et al. Rayleigh instability-assisted satellite droplets elimination in inkjet printing. ACS Appl Mater Interfaces 2017;9:41521–8. https://doi.org/10.1021/acsami.7b11356.
[24] Wang T, Lin J, Lei Y, Guo X, Fu H. Droplets generator: formation and control of main and satellite droplets. Colloids Surf A Physicochem Eng Asp 2018;558:303–12. https://doi.org/10.1016/j.colsurfa.2018.08.046.
[25] Kwon K-S, Kim W. A waveform design method for high-speed inkjet printing based on self-sensing measurement. Sensors Actuators A Phys 2007;140:75–83. https://doi.org/10.1016/j.sna.2007.06.010.
[26] Gan HY, Shan X, Eriksson T, Lok BK, Lam YC. Reduction of droplet volume by controlling actuating waveforms in inkjet printing for micro-pattern formation. J Micromech Microeng 2009;19. https://doi.org/10.1088/0960-1317/19/5/055010.
[27] Yang Z, Tian H, Wang C, Li X, Chen X, Chen X, et al. Piezoelectric drop-on-demand inkjet printing with ultra-high droplet velocity. Research 2023;6:0248. https://doi.org/10.34133/research.0248.
[28] Li EQ, Xu Q, Sun J, Fuh JYH, Wong YS, Thoroddsen ST. Design and fabrication of a PET/PTFE-based piezoelectric squeeze mode drop-on-demand inkjet printhead with interchangeable nozzle. Sensors Actuators A Phys 2010;163:315–22. https://doi.org/10.1016/j.sna.2010.07.014.
[29] Brünahl J, Grishin AM. Piezoelectric shear mode drop-on-demand inkjet actuator. Sensors Actuators A Phys 2002;101:371–82. https://doi.org/10.1016/S0924-4247(02)00212-1.
[30] Kim B-H, Kim S-I, Lee J-C, Shin S-J, Kim S-J. Dynamic characteristics of a piezoelectric driven inkjet printhead fabricated using MEMS technology. Sensors Actuators A Phys 2012;173:244–53. https://doi.org/10.1016/j.sna.2011.10.010.
[31] Shin P, Sung J, Lee MH. Control of droplet formation for low viscosity fluid by double waveforms applied to a piezoelectric inkjet nozzle. Microelectron Reliab 2011;51:797–804. https://doi.org/10.1016/j.microrel.2010.11.017.
[32] Wang GQ, Liao WH, Zhao ZX, Tan JP, Cui SJ, Wu HQ, et al. Nonlinear magnetic force and dynamic characteristics of a tri-stable piezoelectric energy harvester. NONLINEAR DYNAMICS 2019;97:2371–97. https://doi.org/10.1007/s11071-019-05133-z.
[33] Zheng YC, Wang GQ, Zhu QG, Li GB, Zhou YY, Hou LG, et al. Bifurcations and nonlinear dynamics of asymmetric tri-stable piezoelectric vibration energy harvesters. Commun Nonlinear Sci Numer Simul 2023;119. https://doi.org/10.1016/j.cnsns.2022.107077.
[34] Tiersten H. Electroelastic interactions and the piezoelectric equations. J Acoust Soc Am 1981;70:1567–76. https://doi.org/10.1121/1.387222.
[35] Li Y, Liu C, Zou H, Che L, Sun P, Yan J, et al. Integrated wearable smart sensor system for real-time multi-parameter respiration health monitoring. Cell Rep Phys Sci 2023;4:101191. https://doi.org/10.1016/j.xcrp.2022.101191.
[36] Glowinski R, Pironneau O. Finite element methods for Navier-Stokes equations. Annu Rev Fluid Mech 1992;24:167–204. https://doi.org/10.1146/annurev.fl.24.010192.001123.
[37] White JA, Borja RI. Stabilized low-order finite elements for coupled solid-deformation/fluid-diffusion and their application to fault zone transients. Comput Methods Appl Mech Eng 2008;197:4353–66. https://doi.org/10.1016/j.cma.2008.05.015.
[38] Cottet G-H, Maitre E, Milcent T. Level set methods for fluid-structure interaction. Springer Nature; 2022.
[39] Dong H, Carr WW, Morris JF. An experimental study of drop-on-demand drop formation. Phys Fluids 2006;18. https://doi.org/10.1063/1.2217929.
[40] Pimbley W, Lee H. Satellite droplet formation in a liquid jet. IBM J Res Dev 1977;21:21–30. https://doi.org/10.1147/rd.211.0021.